Design and numerical validation of quasi-zero-stiffness metamaterials for very low-frequency band gaps

Changqi Cai[a, b], Jiaxi Zhou[*a, b], Linchao Wu[a], Kai Wang[a, b], Daolin Xu[a, b], Huajiang Ouyang[c]

[a] *State Key Laboratory of Advanced Design and Manufacturing for Vehicle Body, Hunan University, Changsha 410082, PR China,*
[b] *College of Mechanical and Vehicle Engineering, Hunan University, Changsha 410082, PR China,*
[c] *School of Engineering, University of Liverpool, LiverpoolL69 3GH, UK*

Abstract

A novel one-dimensional quasi-zero-stiffness (QZS) metamaterial is proposed to acquire very low-frequency band gaps. The representative unit cell (RUC) of the QZS metamaterials is constructed by combining positive-stiffness (PS) elements (two pairs of folded beams) and negative-stiffness (NS) elements (two pairs of buckled beams) in parallel. The negative stiffness of the buckled beams under large deformation is predicated theoretically by using the elliptic integral method. A parameter design on both the PS and NS elements is carried out, which indicates that the positive stiffness can be substantially neutralized by the NS elements, leading to a QZS RUC with ultra-low stiffness. Additionally, the one-dimensional QZS metamaterials are modelled as a lumped-mass-spring chain, which is solved theoretically by using the Harmonic Balance method, and then the dispersion relations and the band gaps are revealed. This chain model is also solved numerically and validated by finite element analysis. Both the theoretical and numerical predictions show very low-frequency band gaps (about 20Hz). Therefore, the proposed QZS metamaterials should be a promising solution for very low-frequency wave filtering or attenuation.

Keywords: Quasi-zero stiffness; metamaterials; low frequency; band gaps; local resonance.

[*]Corresponding author.
Address: College of Mechanical and Vehicle Engineering, Hunan University, Changsha 410082, PR China.
E-mail address: jxizhou@hnu.edu.cn (Jiaxi Zhou); Telephone number: +86 13975835883.

1. Introduction

In the past three decades, the propagation of elastic or acoustic waves in periodic structure called phononic crystals (PCs) or metamaterials has received much attention [1–4], which exhibits exceptional material properties not observed in nature, i.e., negative mass density or negative Young's modulus. Especially, waves can be attenuated by metamaterials in certain frequency ranges, called stop bands or band gaps [5], which can be applied in vibration isolation, wave attenuation, waveguides，acoustic absorption and etc. [6–14].

There are two formation mechanisms of band gaps called Bragg scattering (BS) and local resonance (LR). The central frequency of BS band gaps is inversely proportional to geometric scale (lattice constant) of the PCs [15]. Hence, it is impractical to open low frequency BS band gaps unless the PCs have a large lattice constant. Fortunately, the work by Liu et al. [16] offered a novel route to generating low-frequency band gaps which is called local resonance (LR).

Recently, several researchers tried to devise some novel local resonant metamaterials to open the band gap at a low frequency. Pai *et al*. [11] designed new metamaterial beam based on multi-frequency vibration absorbers for broad band vibration absorption. Qureshi *et al*. [17] fabricated a 3D-printed cantilever-in-mass structure for creating low-frequency band gaps. Ma *et al*. [18] proposed a periodic vibration suppressor with multiple secondary oscillators for reducing low-frequency vibration. Virgin *et al*. [19] achieved low-frequency band gaps by employing a highly deformed slender beam. Chen *et al*. [20], Wang *et al*. [21], Zhou *et al*. [15] and Yu *et al*. [22] also achieved low-frequency band gaps for flexural waves in beams by local resonators. In addition, Zhong *et al*. [23] proposed an underwater acoustic ultra-thin metamaterial plate embedded with spiral local resonators to obtain excellent underwater sound absorption performance and low-frequency band gaps. For

broadening the frequency range of local resonance band gaps, Wang *et al*. [24] proposed a tuneable digital metamaterial plate with embedded electromagnets. Liu *et al*. [7] also designed a broad band locally resonant metamaterial sandwich plate for noise insulation in the coincidence region.

Moreover, nonlinear locally resonant metamaterials were also used to fulfil low-frequency band gaps or wave manipulation. Meaud *et al*. [25] achieved a low-frequency band gap by architected materials with bistable unit cells. Nadkarni *et al*. [26] proposed a periodic lattice with bistable unit cells connected by magnetic links, which enabled unidirectional transition wave propagation at constant wave velocity. Raney *et al*. [27] presented an architected soft system composed of elastomeric bistable beam elements connected by elastomeric linear springs, for propagation of stable, nonlinear solitary transition waves with constant, controllable velocity and pulse geometry over arbitrary distances. Goldsberrya *et al*. [28] designed a negative-stiffness honeycomb for transverse wave guide depending on static pre-strain levels.

Usually, there are two ways to reduce the resonant frequency further, namely increasing the mass or decreasing the stiffness of the resonator [18, 19]. However, the above methods might be unworkable to open band gaps at very low frequencies, because it is unrealizable to make the stiffness of a resonator ultra-small, or the mass ultra-large. Therefore, it is still a challenge to realize wave attenuation at very low frequencies. Fortunately, the authors' works [29–33] have shown that suitable local resonant structures with high-static-low-dynamic-stiffness (HSLDS) resonators can create a band gap at very low frequency. However, the HSLDS resonator was built by connecting a vertical spring with oblique springs (negative-stiffness mechanism) in parallel, which is not compact enough to implement local resonant metamaterials in small scale.

Generally, the space-consuming negative-stiffness mechanism can be replaced by a

compact bistable elastic structure, which enables negative stiffness by utilizing snap-through buckling. The main contribution of this paper is to devise a new kind of one-dimensional QZS metamaterials by connecting a bistable structure with an elastic element in parallel. In the representative unit cell (RUC) of QZS metamaterials, two pairs of buckled beams provide the longitudinal negative stiffness, while the elastic element, two pairs of multi-segment folded beams, produces the positive stiffness. The positive stiffness can be substantially neutralized by the negative stiffness, which leads to quasi-zero stiffness.

It should be noted that the stiffness of the QZS metamaterials are positive rather than negative for the bistable metamaterials. Therefore, the dynamic systems of the QZS metamaterials are absolutely stable, which can definitely enable a low-frequency band gap, even though the bistable metamaterials have fantastic properties in manipulating wave propagation.

This paper is organized as follows: In section 2, the parameter design on the RUC of the metamaterials is carried out to realize the quasi-zero stiffness. In section 3, the QZS metamaterials are modelled as a damped nonlinear chain. The dispersion relation is derived by the Harmonic Balance method and the band gap is revealed, which is verified by numerical simulations and finite element analysis. The damping, mass ratio and excitation amplitude on the band gap are discussed in Section 4. Finally, some conclusions are drawn in Section 5.

2. Design procedure of QZS metamaterials

The one dimension (1D) QZS metamaterials and their representative unit cell (RUC) are illustrated in Fig. 1. The RUC is composed of four parts, namely supporting frame, positive-stiffness (PS) element, negative-stiffness (NS) element, and central mass, which can be made of the same material by additive manufacturing technology. The

positive-stiffness element contains two pairs of folded beams. One folded beam is made up of five segments of beams with lengths of d, c, a, c and d, as shown in Fig. 1(b). Parameters r and h denote the fillet radii at the corner, and the thickness of the folded beam, respectively. Parameter b denotes the out-plane width of the RUC. The negative-stiffness element consists of two pairs of oblique beams. Buckling occurs when the oblique beams are subjected to compression, which can provide negative stiffness along the longitudinal direction of the 1D metamaterials. The length and thickness of the oblique beam are l and h, respectively. Since the positive-stiffness element is connected in parallel with the negative-stiffness one, the overall stiffness of the RUC can be assigned a desired low value. The central mass is connected with the supporting frame through both the PS and NS elements. In this section, the mechanical features on the RUC are made to fulfil the quasi-zero-stiffness feature.
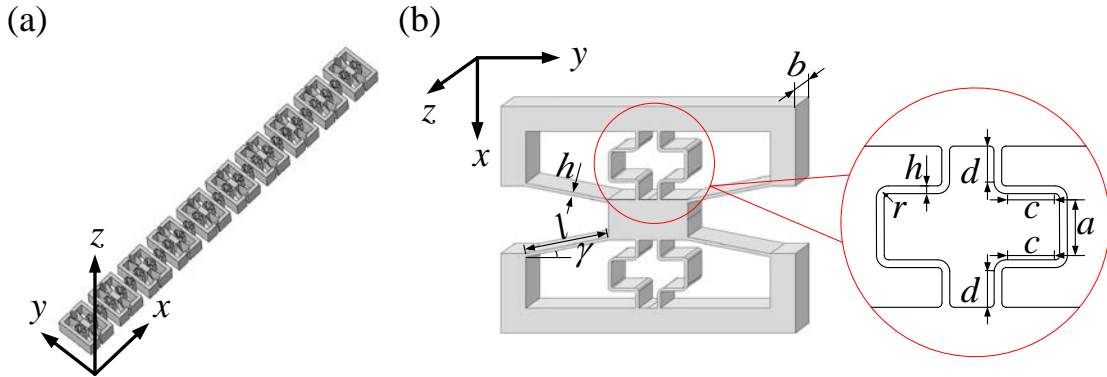
(a)　　　　　　　　　(b)

Fig. 1 Schematic diagrams of (a) the 1D QZS metamaterials and (b) the representative unit cell

Due to the symmetrical configuration, a half of the RUC is taken to study the stiffness feature. Assuming that an external force F_h acts on the central lumped mass, which leads to a vertical displacement x, as shown in Fig. 2(a). The external force F_h is supported by both the positive- and negative-stiffness elements, as shown in Fig. 2(b) and 2c, respectively. The force-displacement relationship, F_h vs x, of the RUC can be obtained by combining those of the positive- and negative-stiffness elements, namely F_p vs x and F_n vs x.
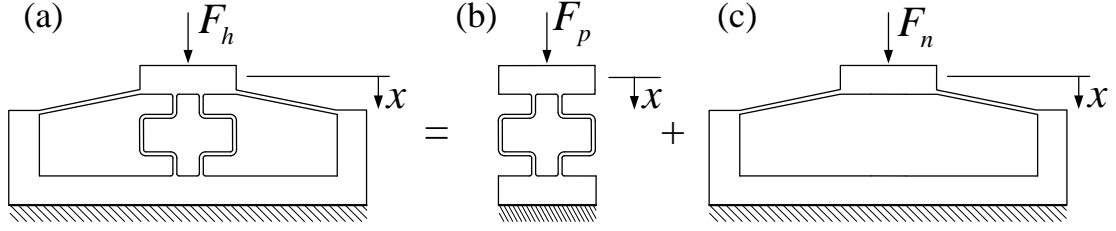
Fig. 2 Schematic diagrams of (a) a half of the RUC, (b) the positive-stiffness element, and (c) the negative-stiffness element.

2.1 Static analysis of the positive-stiffness element

The positive-stiffness element in Fig. 2b is composed of a pairs of folded beams. The stiffness features, namely the relationship between F_p and x, is revealed by Castigliano's theorem under the assumption of small deformation. Since two folded beams are symmetrically arranged, their deformations are assumed to be identical.

The deformation of the folded beam is dominated by bending, and the deformations caused by shear forces and axial forces are neglected. The folded beam is divided into nine segments, and the bending-moment functions along the folded beam can be given by

$$M_i = M_i(M_c, F_c, T_c, \theta_i, y_i) \qquad (i = 1 \sim 9) \tag{1}$$

where M_c, F_c and T_c are the unknown bending moment, axial force and shear force, respectively, as shown in Fig. 3(a). It is worth noting that the shear T_c is 0, which can be derived by static analysis. In addition, y_{2j+1} ($j=0\sim4$) is the distance from the starting point of each straight segment, and θ_{2j} ($j=1\sim4$) is angle between the tangent of the arc segment and the $2j$-1th straight segment, as illustrated in Fig. 3(b), where the bending-moment diagram is also depicted.
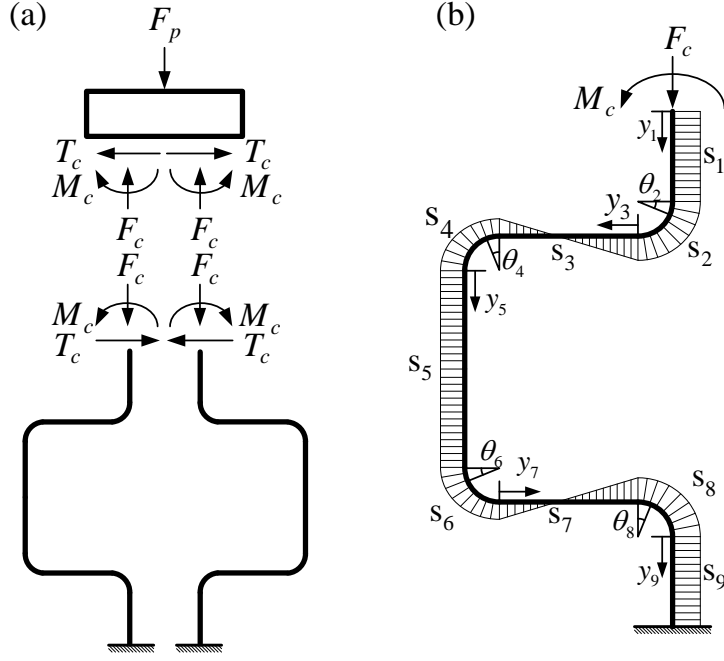
Fig. 3(a) Free-body diagram and (b) bending-moment diagram.

Furthermore, the strain energy of these two folded beams can be written as

$$U = 2\left[\sum_{j=0}^{4}\int_{0}^{l_{2j+1}}\frac{M_{2j+1}^{2}\left(y_{2j+1}\right)}{2EI}dy_{2j+1} + \sum_{j=1}^{4}\int_{0}^{\frac{\pi}{2}}\frac{M_{2j}^{2}\left(\theta_{2j}\right)}{2EI}d\theta_{2j}\right] \tag{2}$$

From the free-body diagram, one can find that $F_c = F_p/2$. According to Castigliano's theorem, and submitting $F_c = F_p/2$ into Eq. (2), the vertical displacement x can be calculated by differentiating the strain energy with respect to the force F_p,

$$x = \frac{\partial U}{\partial F_p} \tag{3}$$

$$= \frac{1}{2EI}\left\{2M_c\left(-2\pi r^2 - 2rc - \pi rc - c^2 - ac - 2ar\right)\right.$$

$$\left. + F_p\left[3\pi r^3 + 6cr^2 + 2\pi cr^2 + 2rc^2 + \pi rc^2 + \frac{2}{3}c^3 + a\left(c+2r\right)^2\right]\right\}$$

Note that M_c cannot be obtained by only the equilibrium equation, and an additional equation is established, based on the boundary condition that the slope of the folded

beam at the beginning end is zero, i.e.

$$
\begin{aligned}
\theta_c &= \frac{\partial(\frac{1}{2}U)}{\partial M_c} \\
&= \frac{1}{EI}\Big\{ M_c\left(a + 2c + 2d + 2\pi r\right) \\
&\qquad - \frac{1}{2}F_p\left[r^2\left(\pi - 2\right) + r\left(2r + \pi c + \pi r\right) + a\left(c + 2r\right) + c^2 + 2cr \right]\Big\} \\
&= 0
\end{aligned}
\tag{4}
$$

From Eq. (4), one can obtain the relationship between M_c and F_p, and then, by substituting M_c into Eq. (3), the relationship between F_p and x can be given by

$$
F_p = \frac{6EI\left(a + 2c + 2d + 2\pi r\right)}{\Pi} x
\tag{5}
$$

where

$$
\begin{aligned}
\Pi &= c^4 + 6r^4\pi^2 + 24c^2r^2 + 2ac^3 + 4c^3d \\
&\quad + 9\pi ar^3 + 30\pi cr^3 + 4\pi c^3 r + 18\pi dr^3 + 6ac^2d \\
&\quad + 18acr^2 + 6ac^2r + 24adr^2 + 36cdr^2 + 12c^2dr \\
&\quad + 3c^2r^2\pi^2 + 24acdr + 6\pi acr^2 + 3\pi ac^2r + 12\pi cdr^2 + 6\pi c^2dr
\end{aligned}
\tag{6}
$$

2.2 Static analysis of the negative-stiffness element

The negative-stiffness element in Fig. 2(c) is composed of a pairs of fixed-guided oblique beams. Under the external compression force F_n, the oblique beams should be designed to achieve the snap-through buckling behaviour, and to realize a bistable flexure mechanism with negative stiffness. The relationship between F_n and x is revealed by the elliptic integral method [34] under large deformation. Due to the symmetrical configuration, the fixed-guided oblique beams undergo the same deformation, as shown in Fig. 4(a).
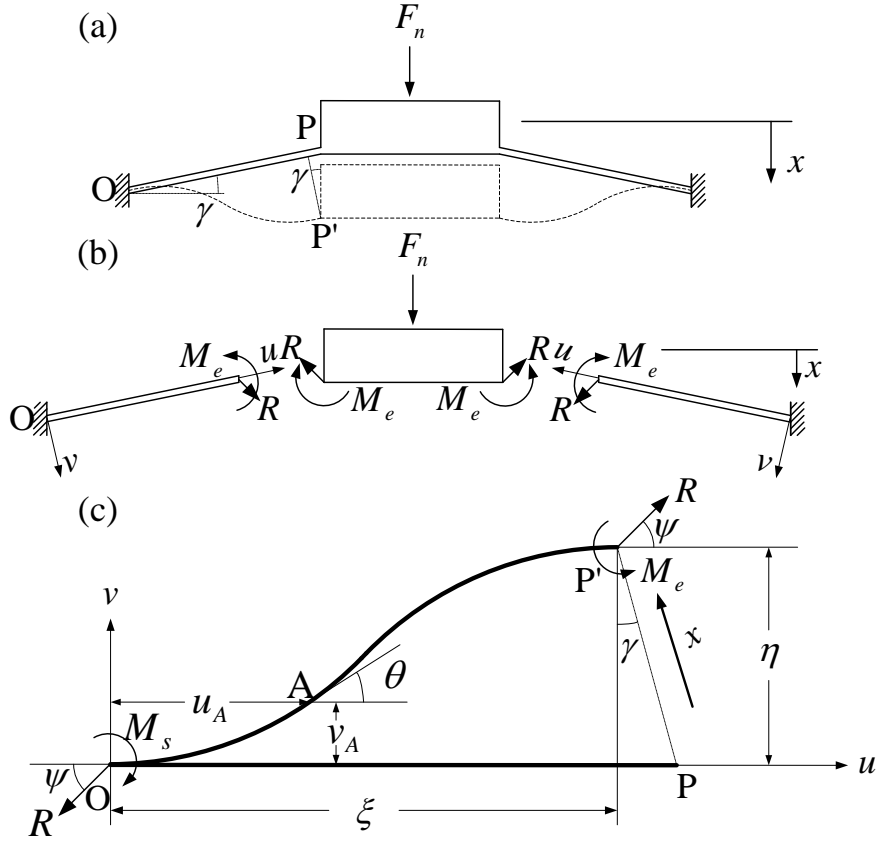
8

Fig. 4 (a) Deformation of the fixed-guided oblique beams, (b) free-body diagram and (c) parameters of the deformed oblique beam.

The bending deflection of the fixed-guided oblique beam is mainly caused by the resultant force R and the moments M_e in Fig. 4(b). Referring to the parameters shown in Fig. 4(c), the Euler-Bernoulli equation for the oblique beam from point O to point A can be given by

$$EI \frac{\mathrm{d}\theta}{\mathrm{d}s} = M_s + Rv_A \cos\psi - Ru_A \sin\psi \tag{7}$$

where u_A and v_A are the horizontal and vertical coordinates of point A in the coordinate system uov, EI is the bending rigidity, ψ is angle of the reaction force R with respect to u, and θ is the slope angle at point A.

By differentiating Eq. (7) with respect to s and using $\cos\theta = \mathrm{d}u_A/\mathrm{d}s$ and $\sin\theta = \mathrm{d}v_A/\mathrm{d}s$, one can yield

$$EI\frac{\mathrm{d}^2\theta}{\mathrm{d}s^2} = R\sin\theta\cos\psi - R\cos\theta\sin\psi \tag{8}$$

Integrating Eq. (8) with respect to θ gives

$$\frac{EI}{2}\left(\frac{\mathrm{d}\theta}{\mathrm{d}s}\right)^2 = -R\cos\theta\cos\psi - R\sin\theta\sin\psi + C \tag{9}$$

where C is a unknown constant. Solving for $\mathrm{d}s$ in Eq. (9) and then integrating from 0 to L result in

$$L = \int_0^L \mathrm{d}s = \int_0^{\theta_m}\frac{\sqrt{EI}}{\sqrt{-2R\cos(\theta-\psi)+2C}}\mathrm{d}\theta + \int_{\theta_m}^0\frac{\sqrt{EI}}{-\sqrt{-2R\cos(\theta-\psi)+2C}}\mathrm{d}\theta \tag{10}$$

where θ_m is the maximum slope angle through the buckled beam.

And the horizontal and vertical displacements of the guided end of the oblique beam can also be given by

$$\eta_b = \int_0^L \sin\theta\mathrm{d}s = \int_0^{\theta_m}\frac{\sqrt{EI}\sin\theta}{\sqrt{-2R\cos(\theta-\psi)+2C}}\mathrm{d}\theta + \int_{\theta_m}^0\frac{\sqrt{EI}\sin\theta}{-\sqrt{-2R\cos(\theta-\psi)+2C}}\mathrm{d}\theta$$

$$\xi_b = \int_0^L \cos\theta\mathrm{d}s = \int_0^{\theta_m}\frac{\sqrt{EI}\cos\theta}{\sqrt{-2R\cos(\theta-\psi)+2C}}\mathrm{d}\theta + \int_{\theta_m}^0\frac{\sqrt{EI}\cos\theta}{-\sqrt{-2R\cos(\theta-\psi)+2C}}\mathrm{d}\theta$$

$$\tag{11}$$

To evaluate these integrals, a constant k and a variable ϕ are introduced

$$C = R(2k^2 - 1) \tag{12}$$

$$\cos(\frac{\psi-\theta}{2}) = k\sin\phi \tag{13}$$

From Eq. (10), one can obtain the relationship between R and k, ϕ. By substituting Eqs. (12) and (13) into Eq. (10), one can yield

$$\sqrt{\mu} = \sqrt{\frac{L^2 R}{EI}} = \int_{\phi_1}^{\phi_2} \frac{\mathrm{d}\phi}{\sqrt{1 - k^2 \sin^2 \phi}} \qquad (14)$$

Note that the value of ϕ changes continuously from ϕ_1 at the left end and ϕ_2 at the right end. For the fixed-guided boundary condition, ϕ_1 and ϕ_2 can be calculated by using

$$\sin \phi_1 = \sin \phi_2 = \frac{1}{k} \cos(\frac{\psi}{2}) \qquad (15)$$

Corresponding to the buckling mode, the relation between ϕ_1 and ϕ_2 can also be described as

$$\phi_2 = n\pi - \phi_1 \quad \text{if } n \text{ is odd} \qquad (16)$$

$$\phi_2 = n\pi + \phi_1 \quad \text{if } n \text{ is even} \qquad (17)$$

For a given ϕ_1, the corresponding ϕ_2 can be determined. Here, only the first two lowest buckling modes are considered during static bending, namely, $n=1$ or 2.

Furthermore, two incomplete elliptic integral functions $G(k, \phi)$ and $H(k, \phi)$ are introduced to solve the integrals, as listed below

$$G(k, \phi) = \int_0^\phi \frac{\mathrm{d}\delta}{\sqrt{1 - k^2 \sin^2 \delta}} \qquad (18)$$

$$H(k, \phi) = \int_0^\phi \sqrt{1 - k^2 \sin^2 \delta} \, \mathrm{d}\delta \qquad (19)$$

Therefore, Eq. (10) and Eq. (11) can be rewritten as

$$\sqrt{\mu} = G(k, \phi_2) - G(k, \phi_1) \qquad (20)$$

$$\frac{\eta_b}{L} = -\frac{1}{\sqrt{\mu}} \left\{ \sin\psi \left[2H(k,\phi_2) - 2H(k,\phi_1) - G(k,\phi_2) + G(k,\phi_1) \right] \right.$$
$$\left. +2k\cos\psi \left(\cos\phi_1 - \cos\phi_2 \right) \right\} \tag{21}$$

$$\frac{\xi_b}{L} = -\frac{1}{\sqrt{\mu}} \left\{ \cos\psi \left[2E(k,\phi_2) - 2E(k,\phi_1) - F(k,\phi_2) + F(k,\phi_1) \right] \right.$$
$$\left. +2k\sin\psi \left(\cos\phi_2 - \cos\phi_1 \right) \right\} \tag{22}$$

Next, the axial deflection of the oblique beam is calculated. According to Hooke's law, the axial strain of the oblique beam can be given by

$$\varepsilon = \frac{R\cos(\psi - \theta)}{EA} \tag{23}$$

Therefore, the vertical and horizontal displacements caused by the axial force at the right end of the beam can be yielded as

$$\frac{\eta_a}{L} = \frac{1}{L} \int_0^L \varepsilon \sin\theta \mathrm{d}s = \frac{\sqrt{\mu}}{\lambda^2} \int_{\phi_1}^{\phi_2} \frac{\cos(\theta - \psi)\sin\theta}{\sqrt{1 - k^2 \sin^2\phi}} \mathrm{d}\phi \tag{24}$$

$$\frac{\xi_a}{L} = \frac{1}{L} \int_0^L \varepsilon \cos\theta \mathrm{d}s = \frac{\sqrt{\mu}}{\lambda^2} \int_{\phi_1}^{\phi_2} \frac{\cos(\theta - \psi)\cos\theta}{\sqrt{1 - k^2 \sin^2\phi}} \mathrm{d}\phi \tag{25}$$

where the slenderness ratio λ is defined as

$$\lambda^2 = \frac{AL^2}{I} \tag{26}$$

By adding the axial and the bending displacements, the total vertical and horizontal displacements of the beam in the coordinate system uov are obtained

$$\eta = \eta_b + \eta_a \tag{27}$$
$$= -\frac{L}{\sqrt{\mu}} \left\{ \sin\psi \left[2H(k,\phi_2) - 2H(k,\phi_1) - G(k,\phi_2) + G(k,\phi_1) \right] \right.$$
$$\left. +2k\cos\psi \left(\cos\phi_1 - \cos\phi_2 \right) \right\} + \frac{L\sqrt{\mu}}{\lambda^2} \int_{\phi_1}^{\phi_2} \frac{\cos(\theta - \psi)\sin\theta}{\sqrt{1 - k^2 \sin^2\phi}} \mathrm{d}\phi$$

$$\xi = \xi_b + \xi_a \tag{28}$$

$$= -\frac{L}{\sqrt{\mu}} \left\{ \cos\psi \left[2E(k,\phi_2) - 2E(k,\phi_1) - F(k,\phi_2) + F(k,\phi_1) \right] \right.$$

$$\left. + 2k\sin\psi(\cos\phi_2 - \cos\phi_1) \right\} + \frac{L\sqrt{\mu}}{\lambda^2} \int_{\phi_1}^{\phi_2} \frac{\cos(\theta-\psi)\cos\theta}{\sqrt{1-k^2\sin^2\phi}} d\phi$$

Eq. (27) and Eq. (28) are two nonlinear algebra equations with respect to four variables η, ξ, k and ψ. For a set of given displacements ξ and η, the variables k and ψ are solved from the nonlinear algebra equations (27) and (28) with MATLAB codes developed by Howell et al. [35]. Once k and ψ are determined, the reaction force R can be calculated by substituting k and ψ into Eq. (14) and Eq. (15). Then, from the free-body diagram in Fig. 4(a), one can derive the relation between F_n and R

$$F_n = -2R\sin(\psi - \gamma) \tag{29}$$

In addition, from the geometrical relation in Fig. 4(c), the displacement x can be given by

$$x = \sqrt{(L-\xi)^2 + \eta^2} \tag{30}$$

As a result, the relationship between the force F_n and the displacement x is determined.

2.3 Stiffness features of the QZS RUC

From Fig. 2, it can be seen that the positive-stiffness element is connected in parallel with the negative-stiffness element. Therefore, one can obtain the relationship between F_h and x,

$$F_h(x) = F_p(x) + F_n(x) \tag{31}$$

Also, the stiffness of a half of the RUC k_h can be given by

$$k_h(x) = k_p(x) + k_n(x) = \frac{dF_p(x)}{dx} + \frac{dF_n(x)}{dx} \tag{32}$$

To acquire a desired low stiffness, the parameters of the negative-stiffness element is kept unchanged, while the geometrical parameter c (Fig. 1(b)) is designed to adjust the positive stiffness, and thus to tune the overall stiffness of the RUC.

The parameters of the RUC are listed in Table 1. Among of these parameters, a, c and d are the lengths of the segments of the folded beam in the positive-stiffness element; r is the radius of the arc segment in the positive-stiffness element; b is the out-plane width of the RUC and h is the in-plane height of all folded and buckled beams; l is the origin length of the buckled beam; and γ is the initial oblique angle of the buckled beam. The restoring force and stiffness are illustrated in Fig. 5. Obviously, the restoring force F_p of the PS element increases monotonically and proportionally with respect to the displacement x, while the restoring force of the NS element firstly rises steeply and then decreases suddenly against x due to the snap-through buckling of the oblique beams. Correspondingly, the stiffness of the PS element is a constant, but that of the NS element reduces dramatically until it suddenly falls towards a negative value, and then nearly remains unchanged as constant. Since the RUC is composed of the PS element connected in parallel with the NS element, the restoring force F_h and stiffness k_h can be achieved by combining those of the PS element and NS element, as represented as solid lines in Fig. 5. It can be seen that the overall restoring force F_h firstly increases steeply and then very slightly in a large displacement range, which implies that a quasi-zero stiffness is realized in such a displacement range.

14

Table 1 Parameters of the RUC

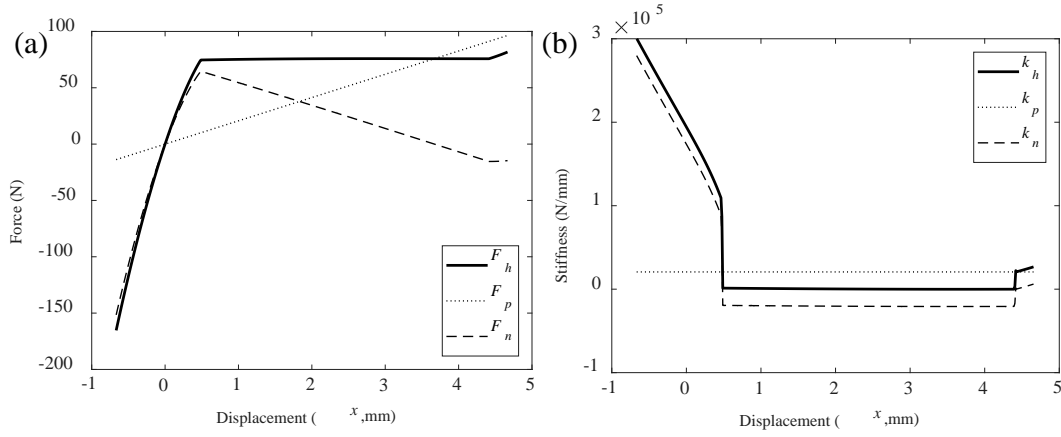| Parameter	Geometrical dimensions (mm)								Material	
	a	c	d	b	l	r	h	γ	E	ρ
Value	5.4	4.75	3.5	25	18.716	0.65	0.7	11.308°	2.3465GPa	1.13kg/m^3

Fig. 5 Stiffness characteristics of half a RUC: (a) relationship between restoring force F_h and

displacement x; (b) relationship between stiffness k_h and displacement x.

Next, the stiffness feature of the whole RUC is presented. To achieve the quasi-zero stiffness, the snap-through buckling of the oblique beam should occur. It is, therefore, necessary to apply a preload on the RUC, as shown in Fig. 6(a). Obviously, under the pre-compression 2Δ, the upper and lower half of the RUC deform in mirror symmetry, and all oblique beams undergo buckling. After preloading, both the upper and lower ends of the RUC are fixed relatively, which means that there is no relative displacement between the upper end of the RUC and the lower one. More importantly, the central mass can move along the vertical direction X freely.
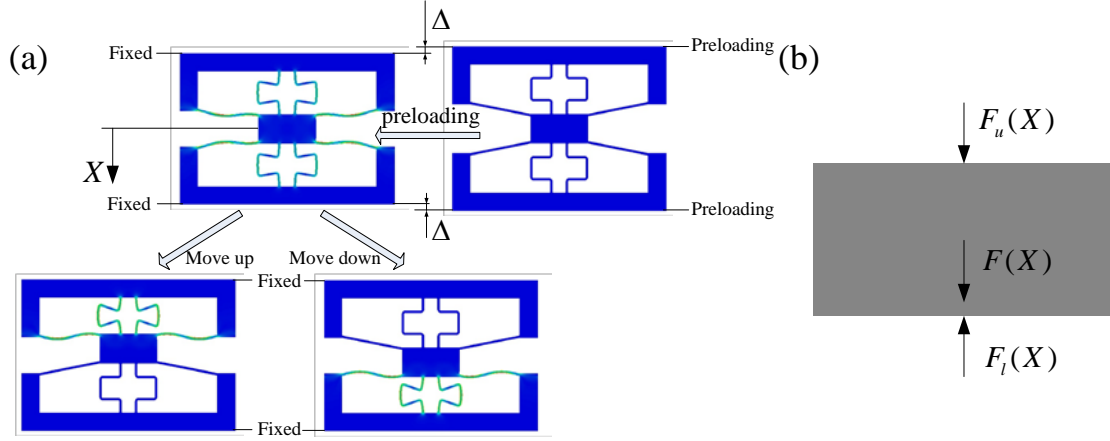
Fig. 6 (a) Preloading process of the RUC and (b) free-body diagram of the central mass

The free-body diagram of the central mass is shown in Fig. 6(b). When the mass moves down by X, the restoring forces by the upper half and the lower half of the RUC are represented by $F_u(X)$ and $F_l(X)$, respectively. Therefore, the restoring force of the RUC F can be given by

$$F(X) = F_l(X) - F_u(X) \tag{33}$$

The restoring forces of the upper and lower halves can be obtained by carrying out coordinate transformations on the restoring force of the lower half in the coordinate system F_h vs x, as given by

$$F_l(X) = F_h(\Delta + x), \quad F_u(X) = F_l(-X) = F_h(\Delta - x) \tag{34}$$

Substituting Eq. (34) into (33) yields

$$F(X) = F_l(X) - F_u(X) = F_h(\Delta + x) - F_h(\Delta - x) \tag{35}$$

By differentiating Eq. (35) with respect to X, the stiffness of the RUC can be yielded

$$k(X) = \frac{\mathrm{d}F_l(X)}{\mathrm{d}X} - \frac{\mathrm{d}F_u(X)}{\mathrm{d}X} = k_h(\Delta + x) + k_h(\Delta - x) \tag{36}$$

16

When the pre-compression is selected as $\Delta = 2\,\mathrm{mm}$, the restoring forces and stiffness are depicted with respect to the displacement X in Fig. 7, where the curves of the lower and upper halves of the RUC are denoted by dotted and dashed lines, respectively, and that of the whole RUC is represented by solid lines. Note that the static characteristics of the RUC are also studied by the finite element method (FEM), which are denoted by circular dots in Fig. 7.
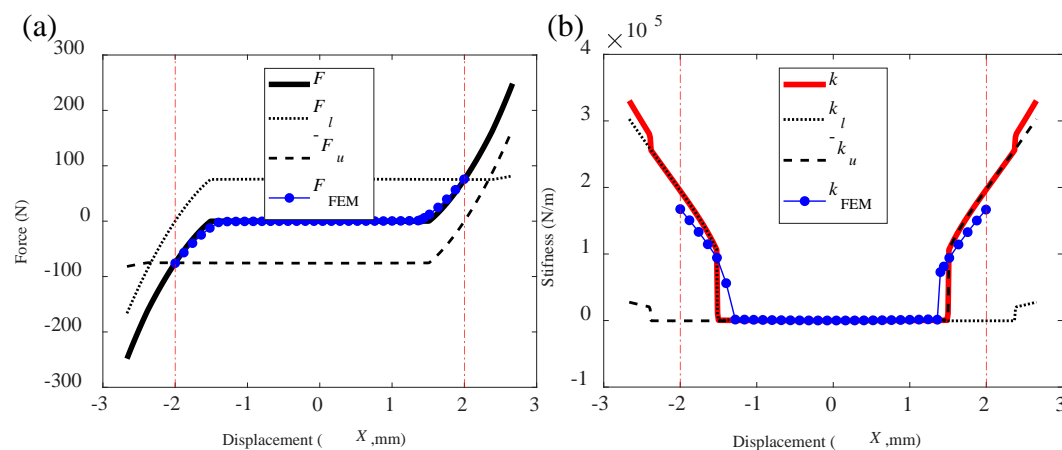

Fig. 7 (a) Restoring force and (b) Stiffness *vs* displacement *X*. Dotted line: lower half RUC, dashed lines: upper half RUC, solid lines: whole RUC, and circular dots: whole RUC by FEM.

Obviously, there is a displacement range where the curve of the restoring force of the RUC is flat, which corresponds to near-zero stiffness; however, the restoring force increases steeply when the displacement is out of such a range, which implies relatively large positive stiffness. This is an ideal stiffness feature for low-frequency vibration attenuation. Ultra-low stiffness is essential to realize low resonant frequency and thus to create low-frequency band gap. However, when the central mass escapes from the displacement rage of quasi-zero stiffness, the increasing stiffness prevents it from undergoing large deflection to avoid structural failure.

More importantly, from Fig. 7, one can also observe good agreement between the analytical restoring forces and stiffness and the numerical ones obtained by FEM, especially in the displacement range of quasi-zero stiffness. Outside of such a range,

17

the theoretical stiffness is somewhat larger than the numerical one, which can be attributed to the assumption of small deformation in theoretical analysis. Overall, the good agreement validates the above design procedure of the QZS RUC.

In summary, the outline of the design procedure can be listed as follows:

- Design the NS element and determine its stiffness feature.
- Design the PS element and adjust its geometrical parameters to tune the overall stiffness of the RUC.
- Apply preloading onto the RUC and the distance between the upper and lower end of the RUC is kept unchanged.

3. Wave attenuation

The quasi-zero-stiffness feature of the 1D metamaterials is realized by parameter design on the RUC composed of positive- and negative-stiffness elements in the above section. In this section, the wave propagation along the QZS 1D metamaterials is investigated and the wave attenuation performance is evaluated by both the lumped-mass chain model and FEM simulations.

3.1 Theoretical prediction of band gaps

3.1.1 Damped nonlinear lumped mass-spring chains system

The one-dimensional QZS metamaterials can be modelled as a spring-mass chain [36], as shown in Fig. 8. In the chain, the supporting frame and central mass are simplified as the lumped masses M and m，respectively, the elastic folded beam between each RUC is represented by spring K, and the PS and NS elements connecting the central mass and the frame is modelled as a nonlinear spring $k_q \, (= k_1 f(u_j - v_j))$ with QZS feature. The parameters of the chain can be determined by the parameters in Table 1 and the stiffness in Fig. 7(b), as shown in Table 2.
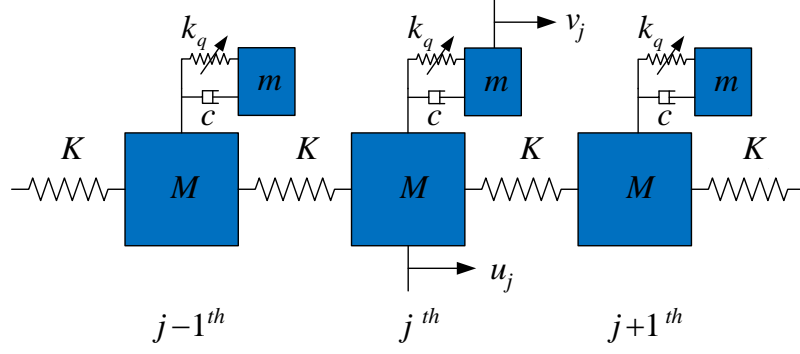
Fig. 8 Simplified spring-mass chains model

Table 2 Parameters of spring-mass chains model

Parameter	M(kg)	m(kg)	K(N/m)	k_1(N/m)	α	β	κ	ζ	χ_1	χ_2
Value	0.0344	0.01	6700	261.7	0.039	0.29	0.37	0.01	-0.04	0.002

When the number of RUCs is large or even infinite, the periodicity of the chain is formed, and any RUC in the chain stays in the same situation. The investigation for any RUC is alike and can reveal all the dynamic characteristics of the whole model. For the jth RUC, the equations of motions can be given by

$$M\ddot{u}_j + 2Ku_j - Ku_{j-1} - Ku_{j+1} + c_1(\dot{u}_j - \dot{v}_j) + k_1 f(u_j - v_j) = 0 \tag{37}$$

$$m\ddot{v}_j + c_1(\dot{v}_j - \dot{u}_j) + k_1 f(v_j - u_j) = 0 \tag{38}$$

where c_1 is the damping coefficient, $k_1 f(v_j - u_j)$ is the nonlinear restoring force, which is shown in Fig. 7(a). To derive the dispersion relationship analytically, the restoring force without explicit expression is fitted by a five-order polynomial

$$f(v_j - u_j) = (v_j - u_j) + \gamma_1(v_j - u_j)^3 + \gamma_2(v_j - u_j)^5 \tag{39}$$

where γ_1 and γ_2 are the parameters representing the degree of nonlinearity.

By introducing the relative displacement $q_j = v_j - u_j$, $\omega_0 = \sqrt{K/M}$ and non-dimensional parameters

$$\tau = \omega_0 t, \hat{u} = \frac{u}{u_s}, \zeta = \frac{c_1}{2\sqrt{k_1 m}}, \hat{q} = \frac{q}{u_s}, \alpha = \frac{k_1}{K}, \beta = \frac{m}{M} \tag{40}$$

where $u_s = 2$mm is displacement of mass M when the stiffness of RUC starts increasing steeply. Then, Eq.(37), (38) and (39) can be rewritten as

$$\hat{u}''_j + 2\hat{u}_j - \hat{u}_{j-1} - \hat{u}_{j+1} - 2\zeta\beta\kappa\hat{q}'_j - \alpha f(\hat{q}_j) = 0 \tag{41}$$

$$\hat{q}''_j + 2\zeta\kappa\hat{q}'_j + \kappa^2 f(\hat{q}_j) + \hat{u}''_j = 0 \tag{42}$$

$$f(\hat{q}_j) = \hat{q}_j + \chi_1\hat{q}_j^3 + \chi_2\hat{q}_j^5 \tag{43}$$

where $\kappa = \dfrac{\sqrt{k_1/m}}{\omega_0} = \sqrt{\dfrac{\alpha}{\beta}}$, is the non-dimensional natural frequency of the linearized

local resonator, $()'$ or $()''$ denote the first- and second-order derivatives with

respect to non-dimensional time τ, respectively, $\chi_1 = \gamma_1 u_s^2$ and $\chi_2 = \gamma_2 u_s^4$.

The equations of motion of the damped nonlinear mass-spring chain are solved by the

Harmonic balance method, and the solution of the jth local resonator is assumed to be

$$\hat{q}_j = B_1 e^{i(\Omega\tau - j\mu)} + \overline{B}_1 e^{-i(\Omega\tau - j\mu)} \tag{44}$$

where $\overline{B}_1$ is conjugate complex number of B_1.

By substituting Eq. (44) into Eq. (42) and integrating twice with respect to time τ,

one can obtain the displacement response of the jth mass M, which is given by

$$\hat{u}_j = B_1[-1 + \frac{2i\zeta\kappa}{\Omega} + \frac{\kappa^2}{\Omega^2}(1 + 3\chi_1 B_1\overline{B}_1 + 10\chi_2 B_1^2\overline{B}_1^2)]e^{i\phi} + c.c. + O(B_1^3 e^{i3\phi}) \tag{45}$$

where $\phi = \Omega\tau - j\mu$, $c.c.$ is the conjugated term about the first term in Eq. (45) and

$O(B_1^3 e^{i3\phi})$ is the term that makes little contribution to the response. Therefore, only

the terms about $e^{i\phi}$ and $e^{-i\phi}$ are preserved in the above expression.

By substituting Eqs. (44) and (45) into Eq. (41) and setting the coefficients of $e^{i\phi}$ to

zero, one can obtain the amplitude-frequency equation

$$[-1+\frac{2i\zeta\kappa}{\Omega}+\frac{\kappa^2}{\Omega^2}(1+3\chi_1 B_1\overline{B}_1+10\chi_2 B_1^2\overline{B}_1^2)](-\Omega^2+2-e^{i\mu}-e^{-i\mu})$$
$$-[2i\zeta\beta\kappa\Omega+\alpha(1+3\chi_1 B_1\overline{B}_1+10\chi_2 B_1^2\overline{B}_1^2)]=0 \tag{46}$$

And then, the dispersion relationship can be derived from Eq. (46)

$$\cos(\mu)=1-\frac{\Omega}{2}-\frac{1}{2}\frac{\Omega^2[2i\zeta\beta\kappa\Omega+\alpha(1+3\chi_1 B_1\overline{B}_1+10\chi_2 B_1^2\overline{B}_1^2)]}{[-\Omega^2+2i\zeta\kappa\Omega+\kappa^2(1+3\chi_1 B_1\overline{B}_1+10\chi_2 B_1^2\overline{B}_1^2)]} \tag{47}$$

The dispersion relation of the chain is depicted in Fig. 9, where the real and imaginary parts of the solution are shown in the right and left planes, respectively. Therefore, the relationship between the wave amplitudes of adjacent masses M_j and M_{j+1} can be demonstrated as

$$\hat{u}_{j+1}=e^{\text{Im}(\mu)}\hat{u}_j e^{-i\text{Re}(\mu)} \tag{48}$$
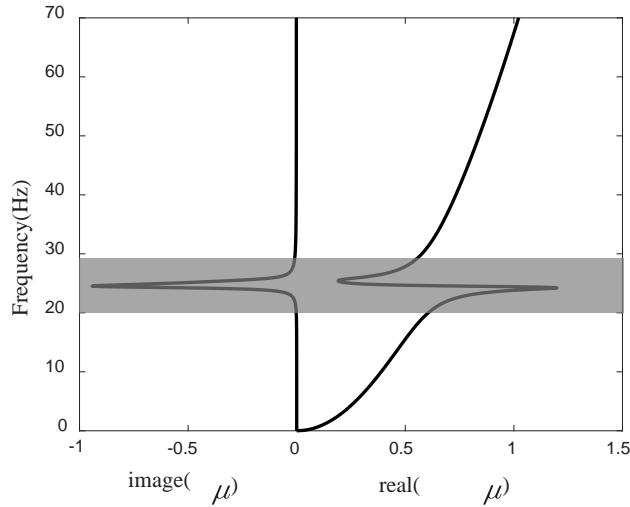

Fig. 9 Nonlinear dispersion relation between frequency and μ

The wave attenuation in the chains occurs in the highlighted grey area (band gap), where attenuation rate $e^{\text{Im}(\mu)}$ is less than 1. The waves at other frequencies outside band gap propagate with little energy loss in the chain and transmission rate $e^{\text{Im}(\mu)}$ is nearly equal to 1. In addition, the phase difference $\text{Re}(\mu)$ of wave propagation

through two neighbour mass M_j and M_{j+1} varies with μ. Inside the band gap, the attenuation rate $e^{\text{Im}(\mu)}$ would be a minimum when $\Omega = \kappa$. In other words, the frequency is equal to the natural frequency of the attached resonator ($\omega = \sqrt{k_1/m}$).

3.1.2 Finite chain

In this section, a finite-length chain with n RUCs is considered, as shown in Fig. 10. The primary spring at the head of the chain connects to the fixed base, while the boundary condition of the tail RUC is free. A harmonic force is applied onto the primary mass M of the first RUC. The equations of motion of the full chain are established, and solved numerically by using Runge-Kutta method. The wave attenuation performance is evaluated in terms of transmittance, which is defined as the horizontal displacement of the first RUC to that of the last one.
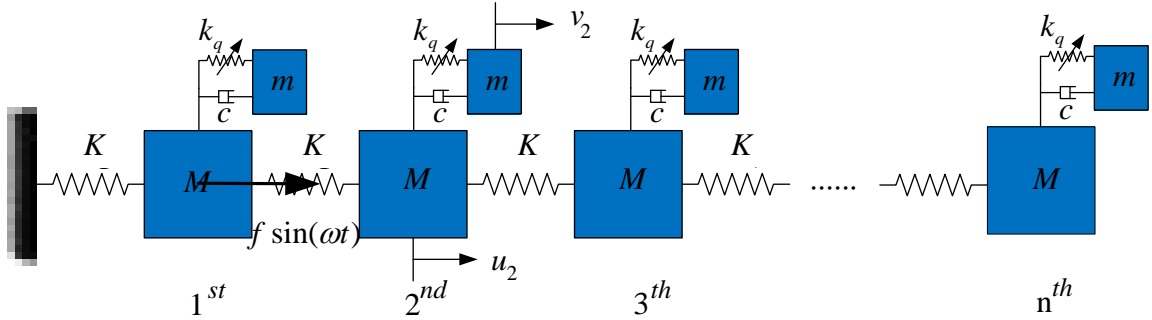

Fig. 10 Schematic diagram of the finite chain

By using the Newton's second law of motion, the equation of motion in matrix form is yielded as

$$\mathbf{M}\ddot{\mathbf{x}} + \mathbf{C}\dot{\mathbf{x}} + \mathbf{F}_k(\mathbf{x}) = \mathbf{F} \tag{49}$$

where $\mathbf{x} = \begin{bmatrix} u_1 & q_1 & u_2 & q_2 & \cdots & u_n & q_n \end{bmatrix}^{\text{T}}$ is the displacement vector, which contains the displacement u_i ($i=1\sim n$) of primary masses and the relative displacements $q_i = u_i - v_i$ ($i=1\sim n$) between the primary mass and the attached oscillator. $\mathbf{M}$ and $\mathbf{C}$ are given by

$$\mathbf{M} = \begin{bmatrix} M & 0 & 0 & 0 & \cdots & 0 & 0 \\ m & m & 0 & 0 & \cdots & 0 & 0 \\ 0 & 0 & M & 0 & \cdots & 0 & 0 \\ 0 & 0 & m & m & \cdots & 0 & 0 \\ \vdots & \vdots & \vdots & \vdots & \ddots & \vdots & \vdots \\ 0 & 0 & 0 & 0 & \cdots & M & 0 \\ 0 & 0 & 0 & 0 & \cdots & m & m \end{bmatrix} \tag{50}$$

$$\mathbf{C} = \begin{bmatrix} 0 & -c_1 & 0 & 0 & \cdots & 0 & 0 \\ 0 & c_1 & 0 & 0 & \cdots & 0 & 0 \\ 0 & 0 & 0 & -c_1 & \cdots & 0 & 0 \\ 0 & 0 & 0 & c_1 & \cdots & 0 & 0 \\ \vdots & \vdots & \vdots & \vdots & \ddots & \vdots & \vdots \\ 0 & 0 & 0 & 0 & \cdots & 0 & -c_1 \\ 0 & 0 & 0 & 0 & \cdots & 0 & c_1 \end{bmatrix} \tag{51}$$

$\mathbf{F} = [f \sin(\omega t) \quad 0 \quad \cdots \quad 0]^{\mathrm{T}}$ is the force vector. There is only one harmonic excitation force acting on the first primary mass M. And $\mathbf{F}_k(x)$ is given by

$$\mathbf{F}_k(x) = \begin{bmatrix} 2K & -k_q & -K & 0 & 0 & \cdots & 0 & 0 & 0 & 0 & 0 & 0 \\ 0 & k_q & 0 & 0 & 0 & \cdots & 0 & 0 & 0 & 0 & 0 & 0 \\ -K & 0 & 2K & -k_q & -K & \cdots & 0 & 0 & 0 & 0 & 0 & 0 \\ 0 & 0 & 0 & k_q & 0 & \cdots & 0 & 0 & 0 & 0 & 0 & 0 \\ \vdots & \vdots & \vdots & \vdots & \vdots & \ddots & \vdots & \vdots & \vdots & \vdots & \vdots & \vdots \\ 0 & 0 & 0 & 0 & 0 & \cdots & -K & 0 & 2K & -k_q & -K & 0 \\ 0 & 0 & 0 & 0 & 0 & \cdots & 0 & 0 & 0 & k_q & 0 & 0 \\ 0 & 0 & 0 & 0 & 0 & \cdots & 0 & 0 & -K & 0 & K & -k_q \\ 0 & 0 & 0 & 0 & 0 & \cdots & 0 & 0 & 0 & 0 & 0 & k_q \end{bmatrix} x \tag{52}$$

where K and k_q is the stiffness of primary and attached spring. It is worthily noting that the stiffness k_q, the forth-order polynomial about displacement x, is piecewise nonlinear, but the coefficients of the odd order polynomial about displacement x are zero, namely

$$k_q = \begin{cases} 261.7 - 2.483 \times 10^8 x^2 + 3.308 \times 10^{14} x^4, & |x| < 0.0014\text{m} \\ -3.878 \times 10^4 + 2.194 \times 10^{10} x^2 - 6.781 \times 10^{14} x^4, & |x| \geq 0.0014\text{m} \end{cases} \tag{53}$$

where the stiffness of attached spring is various when the amplitude of relative

displacement $q_i(i = 1, 2, \cdots, n)$ exceeds critical value, 1.4mm.

Then, the Runge-Kutta method is utilized to solve Eq. (49) when the chain is composed of nine primary masses, and the displacement transmittance is obtained, as shown in Fig. 11. It can be seen that wave attenuation happens in the frequency range from 19Hz to 34Hz, as highlighted by the grey area, which can be regarded as a low-frequency band gap. It can also be found that the numerical band gap of the finite chain matches well with theoretical prediction presented in Fig. 9 for the infinite chain.
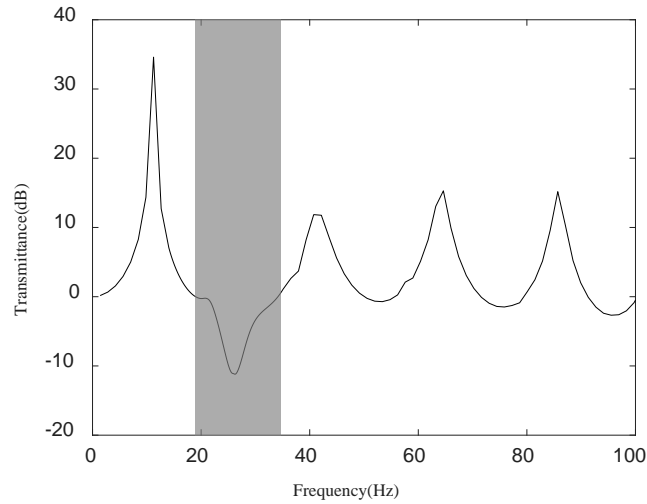

Fig. 11 Displacement transmittance rate of the finite chain

3.2 Band gaps by finite element analysis

To verify the theoretical prediction of the band gap, a finite element (FE) analysis on the finite-length 1D metamaterial is carried out by employing ABAQUS. The FE model of the 1D metamaterial is shown in Fig. 12, which is composed of ten QZS RUCs and nine elastic connecting elements. The boundary conditions of the FE model are similar to the finite chain in Section 3.1.2. The left end of the 1D metamaterial is fixed, while the right end is free. A random excitation acts at the second RUC along the horizontal direction. Each RUC should be pre-compressed to fulfil the quasi-zero stiffness.
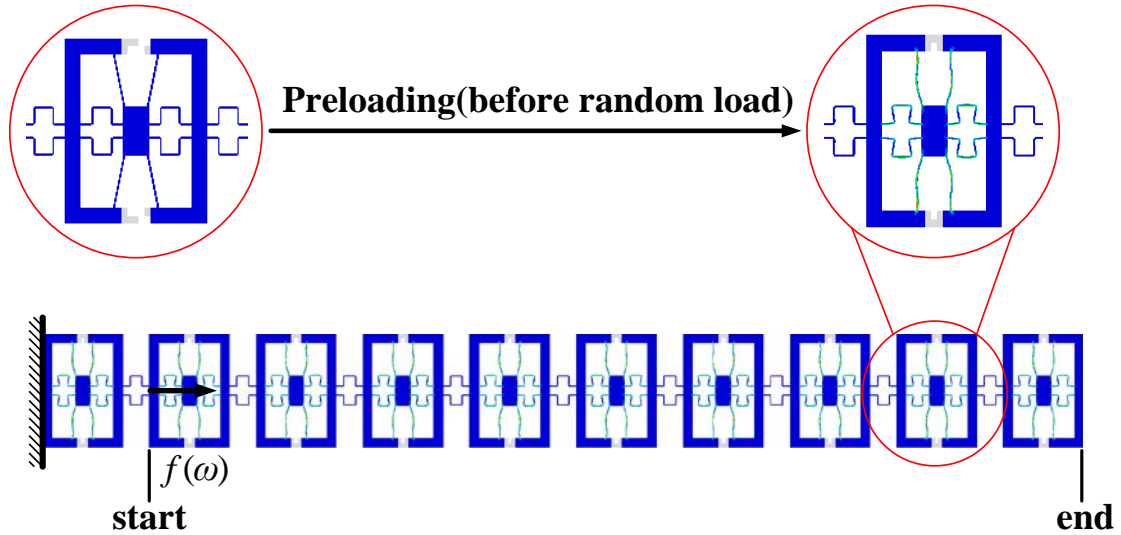
24

Fig. 12 flow-process diagram of FEA

The displacement responses of the starting and ending points are obtained to calculate the displacement transmittance, as demonstrated in Fig. 13. Obviously, in the frequency range from 16Hz to 22Hz, the transmittance (in dB) is below zero, which implies a band gap. Comparing Fig. 13 with Fig. 9 and Fig. 11, one can see that the band gap revealed by the finite element analysis is in good agreement with those predicted both theoretically by using the infinite chain model and numerically by the finite chain model. More importantly, the low-frequency band gap is realized by employing the proposed conceptual design of the QZS metamaterial.
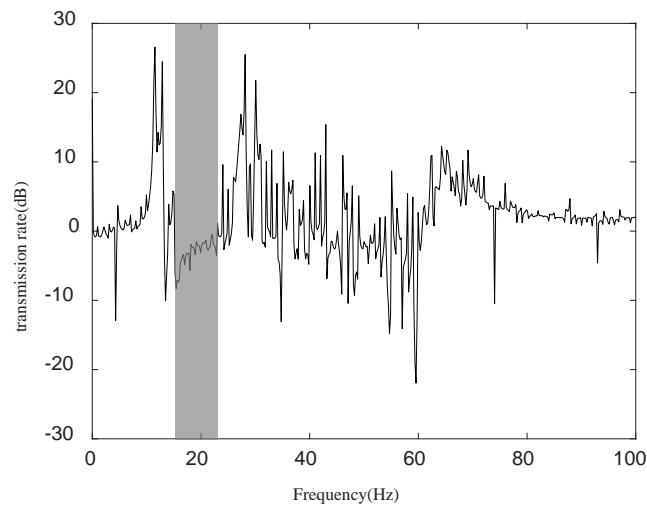

Fig. 13 the displacement transmission rate of FEA model

4. Discussions

From Eq. (47), one can see that the dispersion relation is dependent on the damping ratio ζ, mass ratio β and nonlinearity $\chi_1 B_1 \overline{B}_1$. In this section, the influences of these two parameters on the band gap are discussed by using the finite chain model. The effect of the damping ratio ζ on the band gap is shown in Fig. 14. The band gap is broadened to a wider frequency range with increasing damping, but the depth of the band gap is reduced, which implies that the performance of vibration absorption is degraded. Meanwhile, the center frequency of the band gap is kept unchanged.
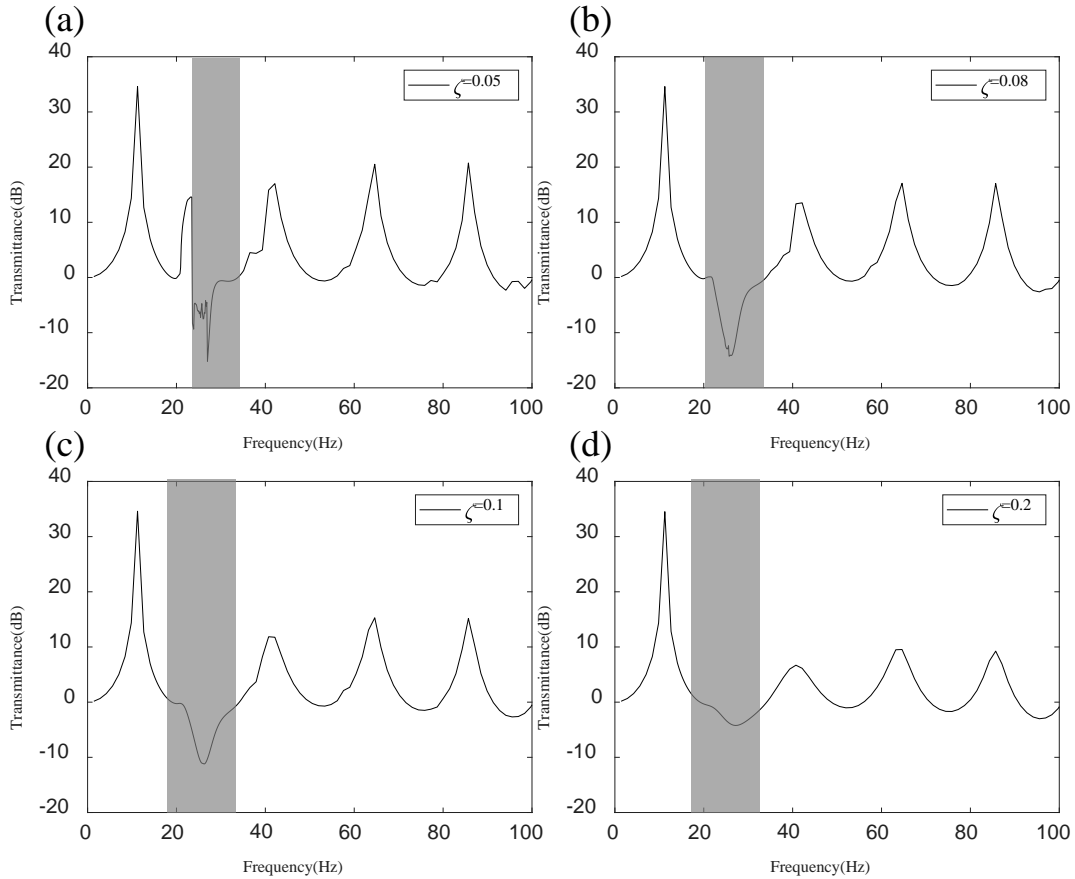

Fig. 14 The relationship of transmittance and frequency for different damping

$(\zeta = 0.05, 0.08, 0.1, 0.2; \alpha = 0.039; \beta = 0.29)$

The influence of the mass ratio β on the transmittance is shown in Fig. 15. The center frequency is equal to the resonant frequency of the local resonator κ ($\sqrt{\alpha/\beta}$),

which is inversely proportional to $\sqrt{\beta}$, and thus the center frequency increases as the
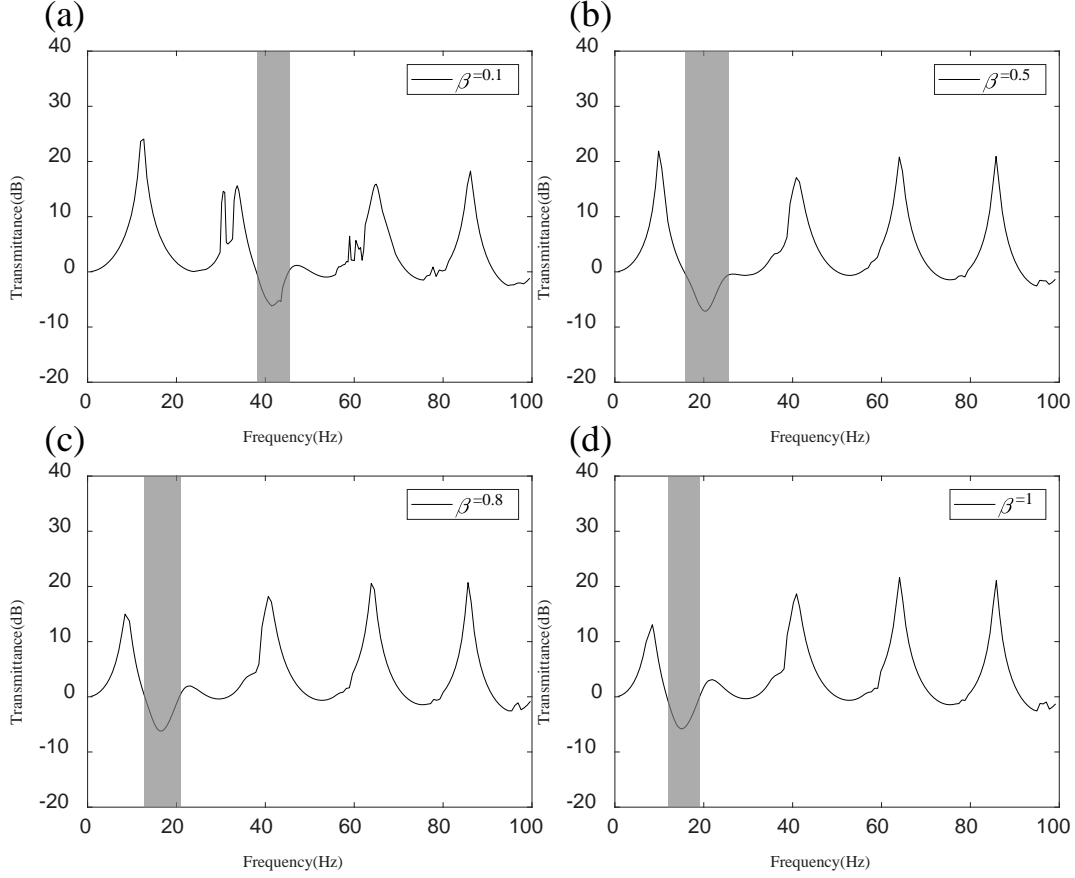
mass ratio β decreases.

Fig. 15 Influence of mass ratio on the transmittance and band gap

($\beta = 0.1, 0.5, 0.8, 1.0; \alpha = 0.039; \zeta = 0.08$)

In order to demonstrate the change of the center frequency against the mass ratio more

clearly, both the numerical and theoretical center frequencies of these 4 cases are

listed in Table 3. The numerical center frequency is defined as the frequency at the

minimum value of the wave transmittance, and the theoretical one is calculated by

$\frac{\omega_0}{2\pi}\sqrt{\alpha/\beta}$. Obviously, when β decreases to 0.5 (from 1 to 0.5), the mass of the

resonator is reduced by a half, and thus the center frequency is increased to $\sqrt{2}$

times theoretically. Similarly, when β decreases to 0.1 (from 1 to 0.1), the center

frequency is increased to $\sqrt{10}$ times theoretically. In such a case, the center

frequency is notably shifted from 15.1Hz to 41.4Hz. Note that there is a difference between the numerical and theoretical center frequencies. For example, the ratio of the numerical center frequency for $\beta = 0.5$ to that for $\beta = 1$ is about 1.35, which is different from but very close to the theoretical value $\sqrt{2}$.

Table 3 Center frequencies of the band gaps in 4 cases

β	0.1	0.5	0.8	1
Numerical center frequency (Hz)	41.40	20.35	16.45	15.10
Theoretical center frequency (Hz)	43.86	19.62	15.51	13.87

All the above cases are under the small displacement. The effect of the excitation amplitude on the transmittance is shown in Fig. 16. Obviously, the band gap is narrowed with the load increasing. This can be attributed to the increasing nonlinearity against the displacement. The stiffness of the QZS metamaterial is nonlinear, which has a stiffness-hardening feature, and the nonlinearity would be enhanced as the displacement is increased. The strong nonlinearity would induce complicated responses, such as sub-harmonic, quasi-periodic and even chaotic motions. The responses at the frequencies in the band gap would be increased substantially, and thus the band gap narrows, and even disappears, as shown in Fig. 16(d). It can also be seen that the beginning frequency of the band gap slightly moves toward a higher frequency and the jump-down phenomenon occurs, due to the increasing stiffness and nonlinearity as the excitation is increased.
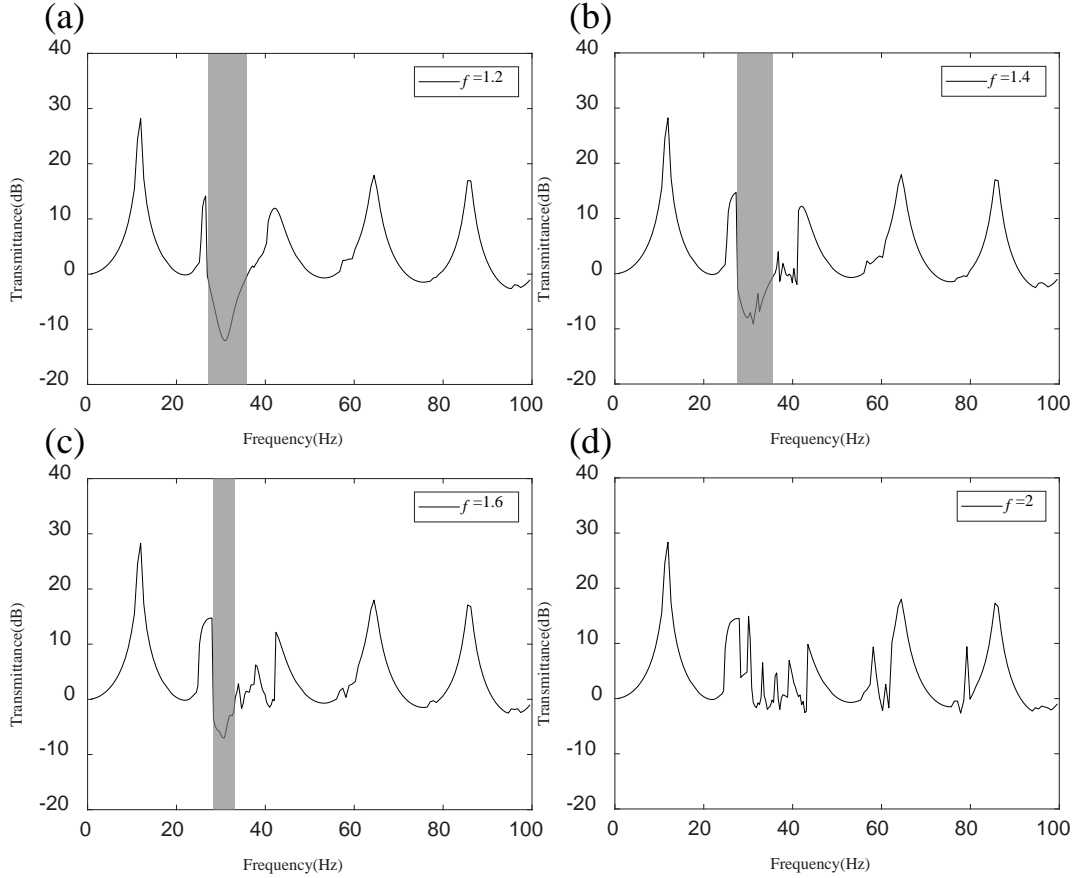
Fig. 16 Influence of excitation amplitude on the transmittance and band gap

($\beta = 0.2; \alpha = 0.039; \zeta = 0.08;\ \ f = 1.2, 1.4, 1.6, 2$)

Conclusions

This paper focuses on the design of quasi-zero-stiffness (QZS) metamaterials and the formation mechanism of ultra-low frequency band gap. The representative unit cell (RUC) of the QZS metamaterial is engineered by combining two pairs of buckled beams and two pairs of folded beams in parallel. The parameters design of the RUC is made to fulfil quasi-zero stiffness. Furthermore, the one-dimensional metamaterial is modelled as a lumped-mass chain to theoretically study its dispersion characteristics and reveal band gaps, which are validated by using the finite element analysis. The effects of damping, mass ratio and excitation amplitude on the band gap are also discussed.

The results show that the negative-stiffness structure (buckled beams) can substantially neutralize the positive stiffness of the folded beams, leading to a desired QZS feature, which enables ultra-low locally resonant band gaps. Damping can broaden the band gap but reduce wave attenuation in the band gap, and the central frequency can be lowered further as the mass ratio is increased. The stiffness nonlinearity is enhanced and thus the dynamic behaviour of the QZS metamaterials becomes complicated, which would degrade wave attenuation, when the excitation is enlarged.

Acknowledgements

Declarations of interest

The authors declare no conflict of interest.

References

[1]   R. Martínez-Sala, J. Sancho, J. V. Sánchez, V. Gómez JL& FM. Sound attenuation by sculpture. Nature 1995;378:241–241. doi:10.1038/378241a0.

[2]   Hussein MI, Leamy MJ, Ruzzene M. Dynamics of Phononic Materials and Structures: Historical Origins, Recent Progress, and Future Outlook. Appl Mech Rev 2014;66:040802. doi:10.1115/1.4026911.

[3]   Ge H, Yang M, Ma C, Lu MH, Chen YF, Fang N, et al. Breaking the barriers: Advances in acoustic functional materials. Natl Sci Rev 2018;5:159–82. doi:10.1093/nsr/nwx154.

[4]   Ma G, Sheng P. Acoustic metamaterials: From local resonances to broad horizons. Sci Adv 2016;2:e1501595–e1501595. doi:10.1126/sciadv.1501595.

[5]   Nadkarni N, Daraio C, Kochmann DM. Dynamics of periodic mechanical structures containing bistable elastic elements: From elastic to solitary wave propagation. Phys Rev E - Stat Nonlinear, Soft Matter Phys 2014;90:1–13. doi:10.1103/PhysRevE.90.023204.

[6]   Morvaridi M, Carta G, Brun M. Platonic crystal with low-frequency locally-resonant spiral

structures : wave trapping , transmission amplification , shielding and edge waves. J Mech Phys Solids 2018;121:496–516. doi:10.1016/j.jmps.2018.08.017.

[7]   Liu Z, Rumpler R, Feng L. Broadband locally resonant metamaterial sandwich plate for improved noise insulation in the coincidence region. Compos Struct 2018:S0263822318303520. doi:10.1016/j.compstruct.2018.05.033.

[8]   Lee T, Iizuka H. Bragg scattering based acoustic topological transition controlled by local resonance. Phys Rev B 2019;99:064305. doi:10.1103/PhysRevB.99.064305.

[9]   Matlack KH, Bauhofer A, Krödel S, Palermo A, Daraio C. Composite 3D-printed meta-structures for low frequency and broadband vibration absorption. Proc Natl Acad Sci 2016:201600171. doi:10.1073/pnas.1600171113.

[10]   Wang X, Luo X, Zhao H, Huang Z. Acoustic perfect absorption and broadband insulation achieved by double-zero metamaterials. Appl Phys Lett 2018;112:021901. doi:10.1063/1.5018180.

[11]   Pai PF, Peng H, Jiang S. Acoustic metamaterial beams based on multi-frequency vibration absorbers. Int J Mech Sci 2014;79:195–205. doi:10.1016/j.ijmecsci.2013.12.013.

[12]   Xu X, Barnhart M V., Li X, Chen Y, Huang G. Tailoring Vibration Suppression Bands with Hierarchical Metamaterials Containing Local Resonators. J Sound Vib 2018;442:237–48. doi:10.1016/j.jsv.2018.10.065.

[13]   Dai H, Xia B, Yu D. Dirac cones in two-dimensional acoustic metamaterials. J Appl Phys 2017;122:065103. doi:10.1063/1.4998438.

[14]   Zhang P, Wei P, Li Y. The elastic wave propagation through the finite and infinite periodic laminated structure of micropolar elasticity. Compos Struct 2018:S0263822317328489. doi:10.1016/j.compstruct.2018.05.095.

[15]   Zhou J, Wang K, Xu D, Ouyang H. Multi-low-frequency flexural wave attenuation in Euler–Bernoulli beams using local resonators containing negative-stiffness mechanisms. Phys Lett Sect A Gen At Solid State Phys 2017;381:3141–8. doi:10.1016/j.physleta.2017.08.020.

[16]   Liu Z, Zhang X, Mao Y, Zhu YY, Yang Z, Chan CT, et al. Locally resonant sonic materials. Science (80-) 2000;289:1734–6. doi:10.1016/S0921-4526(03)00487-3.

[17]   Qureshi A, Li B, Tan KT. Numerical investigation of band gaps in 3D printed cantilever-in-mass metamaterials. Sci Rep 2016;6:28314. doi:10.1038/srep28314.

[18]   Ma J, Sheng M, Guo Z, Qin Q. Dynamic analysis of periodic vibration suppressors with multiple secondary oscillators. J Sound Vib 2018;424:94–111. doi:10.1016/j.jsv.2018.03.002.

[19]   Virgin LN, Santillan ST, Plaut RH. Vibration isolation using extreme geometric nonlinearity. J Sound Vib 2008;315:721–31. doi:10.1016/j.jsv.2007.12.025.

[20]   Chen JS, Journal CTS, Structures S. Wave propagation in sandwich structures with resonators and periodic cores. J Sandw Struct Mater 2013;15:359–74. doi:10.1177/1099636212468738.

[21]   Wang T, Sheng MP, Qin QH. Multi-flexural band gaps in an Euler-Bernoulli beam with lateral local resonators. Phys Lett Sect A Gen At Solid State Phys 2016;380:525–9. doi:10.1016/j.physleta.2015.12.010.

[22]   Yu D, Liu Y, Wang G, Zhao H, Qiu J. Flexural vibration band gaps in Timoshenko beams with locally resonant structures. J Appl Phys 2006;100:124901. doi:10.1063/1.2400803.

[23]   Zhong H, Gu Y, Bao B, Wang Q, Wu J. 2D underwater acoustic metamaterials incorporating a combination of particle-filled polyurethane and spiral-based local resonance mechanisms. Compos Struct 2019;220:1–10. doi:10.1016/j.compstruct.2019.03.091.

[24] Wang Z, Zhang Q, Zhang K, Hu G. Tunable Digital Metamaterial for Broadband Vibration Isolation at Low Frequency. Adv Mater 2016;28:9857–61. doi:10.1002/adma.201604009.

[25] Meaud J, Che K. Tuning elastic wave propagation in multistable architected materials. Int J Solids Struct 2017;122–123:69–80. doi:10.1016/j.ijsolstr.2017.05.042.

[26] Nadkarni N, Arrieta AF, Chong C, Kochmann DM, Daraio C. Unidirectional Transition Waves in Bistable Lattices. Phys Rev Lett 2016;116:1–5. doi:10.1103/PhysRevLett.116.244501.

[27] Raney JR, Nadkarni N, Daraio C, Kochmann DM, Lewis JA, Bertoldi K. Stable propagation of mechanical signals in soft media using stored elastic energy. Proc Natl Acad Sci 2016;113:9722–7. doi:10.1073/pnas.1604838113.

[28] Goldsberry BM, Haberman MR. Negative stiffness honeycombs as tunable elastic metamaterials. J Appl Phys 2018;123:091711. doi:10.1063/1.5011400.

[29] Wang K, Zhou J, Xu D, Ouyang H. Lower band gaps of longitudinal wave in a one-dimensional periodic rod by exploiting geometrical nonlinearity. Mech Syst Signal Process 2019;124:664–78. doi:10.1016/j.ymssp.2019.02.008.

[30] Wang K, Zhou J, Cai C, Xu D, Ouyang H. Mathematical modeling and analysis of a meta-plate for very low-frequency band gap. Appl Math Model 2019;73:581–97. doi:10.1016/j.apm.2019.04.033.

[31] Zhou J, Dou L, Wang K, Xu D, Ouyang H. A nonlinear resonator with inertial amplification for very low-frequency flexural wave attenuations in beams. Nonlinear Dyn 2019. doi:10.1007/s11071-019-04812-1.

[32] Zhou J, Wang K, Xu D, Ouyang H. Local resonator with high-static-low-dynamic stiffness for lowering band gaps of flexural wave in beams. J Appl Phys 2017;121:044902. doi:10.1063/1.4974299.

[33] Wang K, Zhou J, Wang Q, Ouyang H, Xu D. Low-frequency band gaps in a metamaterial rod by negative-stiffness mechanisms: Design and experimental validation. Appl Phys Lett 2019;114:251902. doi:10.1063/1.5099425.

[34] Holst GL, Teichert GH, Jensen BD. Modeling and Experiments of Buckling Modes and Deflection of Fixed-Guided Beams in Compliant Mechanisms. J Mech Des 2011;133:051002. doi:10.1115/1.4003922.

[35] Howell LL ;Spencer PM. Handbook of Compliant Mechanisms. 1st ed. Wiley; 2013.

[36] Lazarov BS, Jensen JS. Low-frequency band gaps in chains with attached non-linear oscillators. Int J Non Linear Mech 2007;42:1186–93. doi:10.1016/j.ijnonlinmec.2007.09.007.